Energy & Environmental Science

ROYAL SOCIETY OF CHEMISTRY

COMMUNICATION

Cite this: *Energy Environ. Sci.*, 2022, **15**, 2858

Received 17th February 2022,
Accepted 19th May 2022

DOI: 10.1039/d2ee00548d

rsc.li/ees

Structure-controlled graphene electrocatalysts for high-performance H_2O_2 production†

Kyungbin Lee, ‡[a] Jeonghoon Lim, ‡[a] Michael J. Lee, [a] Kun Ryu,[a] Hoyoung Lee, [a] Jin Young Kim, [b] Hyunchul Ju,[c] Hyun-Seok Cho, [d] Byung-Hyun Kim, [e] Marta C. Hatzell, *[a] Joonhee Kang*[ef] and Seung Woo Lee *[a]

Metal-free carbon materials have emerged as cost-effective and high-performance catalysts for the production of hydrogen peroxide (H_2O_2) through the two-electron oxygen reduction reaction (ORR). Here, we show that 3D crumpled graphene with controlled oxygen and defect configurations significantly improves the electrocatalytic production of H_2O_2. The crumpled graphene electrocatalyst with optimal defect structures and oxygen functional groups exhibits outstanding H_2O_2 selectivity of 92–100% in a wide potential window of 0.05–0.7 V *vs.* reversible hydrogen electrode (RHE) and a high mass activity of 158 A g^{-1} at 0.65 V *vs.* RHE in alkaline media. In addition, the crumpled graphene catalyst showed an excellent H_2O_2 production rate of 473.9 mmol $gcat^{-1}$ h^{-1} and stability over 46 h at 0.4 V *vs.* RHE. Moreover, density functional theory calculations revealed the role of the functional groups and defect sites in the two-electron ORR pathway through the scaling relation between OOH and O adsorption strengths. These results establish a structure-mechanism-performance relationship of functionalized carbon catalysts for the effective production of H_2O_2.

Broader context

Hydrogen peroxide (H_2O_2) is an environmentally friendly and economical oxidizing agent used in a variety of applications. The two-electron oxygen reduction reaction ($2e^-$ ORR) is a promising route for H_2O_2 production as an alternative to the current multi-step and energy-intensive anthraquinone oxidation process. However, the performance of conventional catalysts for the $2e^-$ ORR is insufficient to meet industrial demands. It is essential to design highly efficient electrocatalysts with low-cost materials for the on-site production of H_2O_2. Here, the $2e^-$ ORR mechanism and the performance of 3D crumpled graphene catalysts with controlled oxygen functional groups and defect sites is studied. Systematic structural control of graphene catalysts provides synergistic active sites containing oxygen functional groups and defect sites for efficient $2e^-$ ORR. Structure-controlled graphene catalysts enable outstanding activity, selectivity, and stability performance for $2e^-$ ORR and provide a fundamental understanding of the structure–mechanism–performance relationship of metal-free carbon catalysts for efficient H_2O_2 production.

Introduction

With rising concern about environmental degradation, there has been increasing interest in the cost-effective production of hydrogen peroxide (H_2O_2), an environmentally friendly oxidizing agent.[1] H_2O_2 is an important chemical in a variety of industries, including textile manufacturing, disinfectants, semiconductor cleaning, and oilfield sludge and sulfide treatment.[2–6] In addition, H_2O_2 can be a potential energy carrier to generate electricity in fuel cells as an alternative to hydrogen.[7,8] The global H_2O_2 market demand was 4.5 million metric tons in 2020 and the market demand is projected to increase to 5.7 million metric tons by 2027.[9] However, industrial production of H_2O_2 is dependent on the energy-intensive anthraquinone oxidation process (AOP), which requires large infrastructure, generates chemical waste, and makes on-site H_2O_2 production difficult.[10] Direct synthesis of H_2O_2 through the atom economy method provides a facile route to replace the conventional AOP, but it could result in possible explosions

[a] George W. Woodruff School of Mechanical Engineering, Georgia Institute of Technology, Atlanta, GA 30332, USA. E-mail: marta.hatzell@me.gatech.edu, seung.lee@me.gatech.edu
[b] Center for Hydrogen-Fuel Cell Research, Korea Institute of Science and Technology (KIST), Hwarang-ro 14-gil 5, Seongbuk-gu, Seoul 02792, Republic of Korea
[c] Department of Mechanical Engineering, Inha University, 100 Inha-ro Michuhol-Gu, Incheon, 22212, Republic of Korea
[d] Hydrogen Research Department, Korea Institute of Energy Research, 152 Gajeong-ro, Yuseong-gu, Daejeon 34129, Republic of Korea
[e] Computational Science & Engineering Laboratory, Korea Institute of Energy Research, 152 Gajeong-ro, Yuseong-gu, Daejeon 34129, Republic of Korea
[f] Department of Nanoenergy Engineering, Pusan National University, 2 Busandaehak-ro 63beon-gil, Geumjeong-gu, Busan 46241, Republic of Korea. E-mail: j.kang@pusan.ac.kr

† Electronic supplementary information (ESI) available: Fig. S1–S18. See DOI: https://doi.org/10.1039/d2ee00548d

‡ These authors contributed equally to this work.

from the hydrogen and oxygen gas mixture and has limited efficiency.[11,12] Recently, direct H_2O_2 production through electrochemical reduction of oxygen has attracted attention due to its high efficiency, sustainability, inhibition of hazardous transportation, and environmentally benign on-site H_2O_2 production capability under ambient conditions.[13–16] In principle, the electrochemical reduction of oxygen molecules produces H_2O_2 or H_2O *via* the two-electron ($2e^-$) oxygen reduction reaction (ORR, eqn (1)) or four-electron ($4e^-$) ORR pathways (eqn (2)), respectively.[5,17]

$$O_2 + 2H^+ + 2e^- \rightarrow H_2O_2\ E^\circ = 0.70\ \text{V}\ \textit{vs.}\ \text{RHE} \quad (1)$$

$$O_2 + 4H^+ + 4e^- \rightarrow 2H_2O\ E^\circ = 1.23\ \text{V}\ \textit{vs.}\ \text{RHE} \quad (2)$$

E° is the standard equilibrium reaction potential for each pathway and RHE is the reversible hydrogen electrode.[18] The $2e^-$ ORR pathway includes only OOH* intermediate, while the $4e^-$ ORR pathway involves additional O* and OH* intermediates after reduction of OOH*.[19,20] Therefore, efficient electrochemical H_2O_2 production requires cathode catalysts with high selectivity to prevent further reduction water. An ideal catalyst also should exhibit high activity, and stability to enable industrial adaption.

Some noble metals such as Au, Pd, Pt, Pd–Hg, and Au–Pd have shown high activity and selectivity for the $2e^-$ ORR with a low overpotential.[13,21–24] However, the high cost and embodied carbon footprint of noble metals hinders their large-scale application. Introducing a very small amount of metal in carbon materials can generate active metal–nitrogen–carbon (M–N–C) sites for the ORR.[25–27] The activity and selectivity of M–N–C catalysts can be controlled by tuning the metal composition and the surrounding atomic structure of the metal centers.[25,28] Co–N–C catalysts show higher activity and selectivity for $2e^-$ ORR than other M–N–C catalysts because they have weak binding between Co and O_2.[25,28,29] Nevertheless, fine-tuning the coordination structures in M–N–C catalysts is challenging as their synthesis method relies heavily on simple impregnation and reduction processes with toxic NH_3 gas.[25,26] Recently, metal-free carbon-based catalysts have shown great potential as alternative catalysts for H_2O_2 production due to their low cost, high activity, tunability, and excellent stability.[17,30–35] In particular, carbon catalysts containing certain surface oxygen and nitrogen groups have shown highly selective H_2O_2 electrosynthesis in alkaline media.[17,35,36] For example, oxidized carbon nanotubes and reduced graphene oxides with oxygen functional groups on their surface showed high selectivity and catalytic activity for $2e^-$ ORR.[17,35] Additionally, the pyrrolic-N group promotes H_2O_2 production in nitrogen-rich graphene with few layers.[36] However, most carbon-based catalysts showed a narrow overpotential window ($\leq$0.4 V *vs.* RHE) for maintaining high peroxide selectivity.[17,33,34] Furthermore, the structure-mechanism-performance relationship for metal-free carbon catalysts, which is related to their specific functional groups, morphology, and defect structure in carbon, has not been established.

In this study, we prepare a series of oxidized crumpled graphene (OCG) catalysts with adjustable morphologies, oxygen functional groups, and surface defects to establish the structure-mechanism-performance relationship for functionalized carbon catalysts. Various particle sizes, oxygen functional groups, and defect structures of the 3D-structured OCG catalysts are systematically controlled *in situ* using the aerosol spray drying process at different annealing temperatures. 2D graphene-based catalysts can reduce the surface area and block the diffusion pathway for O_2 due to the restacking of graphene sheets. However, this unique 3D structure can increase the electrochemically active surface area as well as decrease the mass transport resistance for efficient ORR. OCG synthesized at 800 °C (denoted as OCG-800) has the optimized oxygen functional groups and defect structure, exhibiting the highest H_2O_2 selectivity (>92%) over a wide range of potential (0.05–0.7 V *vs.* RHE) in alkaline media. In addition, the OCG-800 catalyst delivers a high H_2O_2 productivity of 473.9 mmol $gcat^{-1}$ h^{-1} and excellent stability over 46 h during the chronoamperometry test at 0.4 V *vs.* RHE. Furthermore, density functional theory (DFT) computations reveal the ORR mechanism of OCG electrocatalysts and the role of functional groups and defect sites in the $2e^-$ transfer reaction pathway. The results shed light on the structure-mechanism-performance relationship of functionalized carbon catalysts for the $2e^-$ ORR and provide important insights for the design of metal-free carbon catalysts with controlled functional groups and defect structures for efficient production of H_2O_2.

Results and discussion

Characterization of OCG catalysts

OCG was synthesized using a one-step aerosol spray drying process (Fig. S1, ESI†).[37] The prepared graphene oxide (GO) solution was diluted in deionized water (~1 mg mL^{-1}) and sprayed with an ultrasonic nebulizer to form GO droplets. The resulting GO droplets were passed through a preheated tubular furnace with argon gas at a flow rate of ~1 L min^{-1}. The preheated temperature was set to a controlled reduction temperature from 250 to 1000 °C. The GO sheets accumulated on the surface of the droplets during the annealing process and rapidly shrunk into 3D-shaped OCG owing to the capillary compression force during rapid water evaporation.[38] The physical morphologies of OCGs synthesized at different temperatures (250, 500, 800, and 1000 °C) were investigated by scanning electron microscopy (SEM), transmission electron microscopy (TEM), and high-resolution TEM (HRTEM) analysis of the *d*-spacing profiles. The resultant OCG particles showed a 3D crumpled ball-like shape consisting of smooth surfaces and sharp ridges (Fig. 1a, b and Fig. S2, ESI†). The SEM images of the OCGs showed particle sizes of 720 ± 132 nm for OCG-250, 578 ± 123 nm for OCG-500, 502 ± 82 nm for OCG-800, and 422 ± 98 nm for OCG-1000, with more ridges at higher annealing temperatures. Narrow ridge regions were formed by the restacking of graphene sheets, as shown in the HRTEM

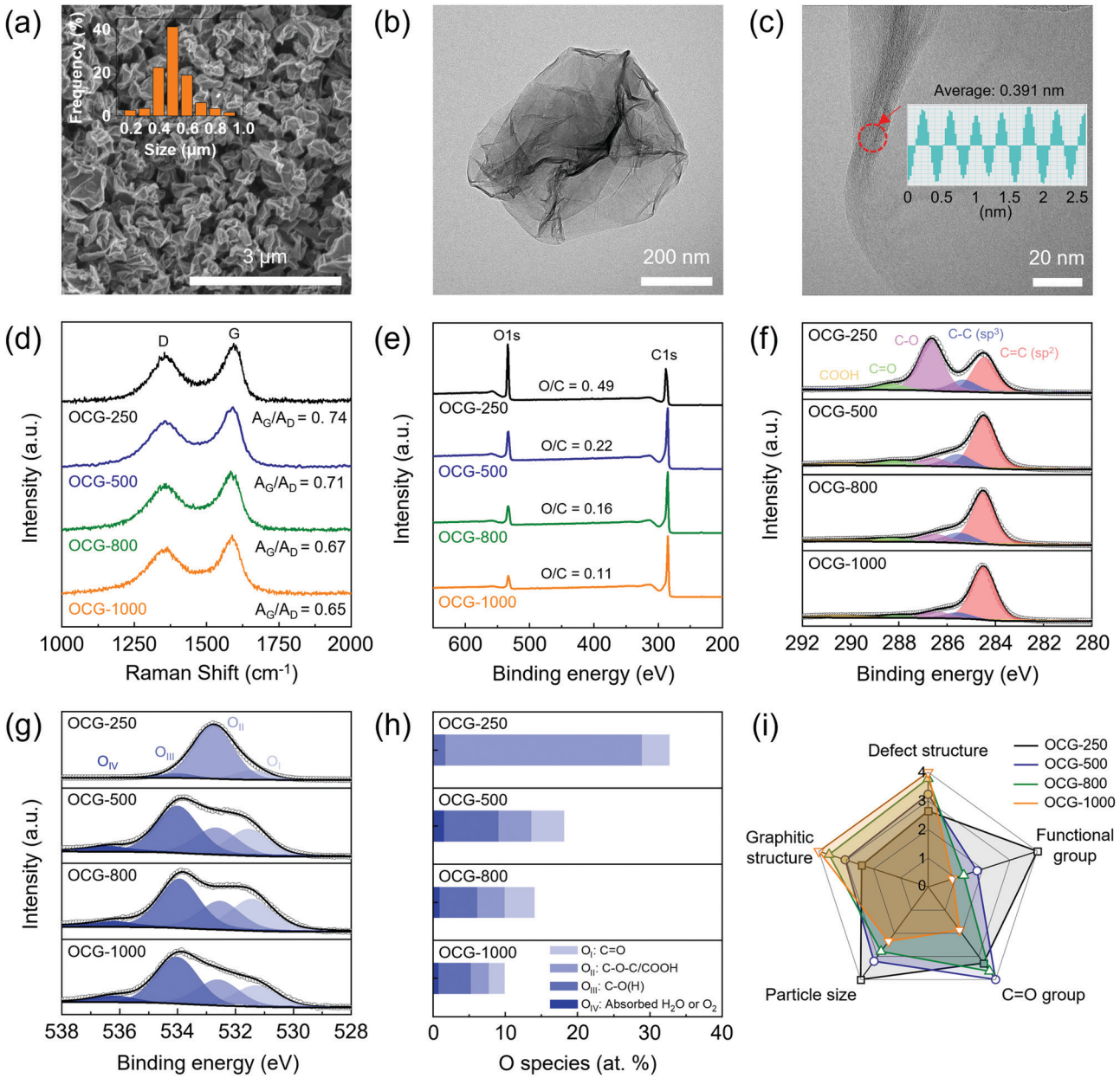

Fig. 1 (a) Scanning electron microscopy (SEM, Inset: size distribution of the particles), (b) transmission electron microscopy (TEM), and (c) high-resolution TEM (HRTEM) with *d*-spacing profiles of OCG-800. (d) Raman spectra, (e) survey scan of X-ray photoelectron spectroscopy (XPS), high resolution (f) C1s, (g) O1s XPS spectra, and (h) atomic percentages of oxygen species of OCG particles synthesized at different reduction temperatures from 250 to 1000 °C. (i) Radar plot comparing the physical and chemical structures of various OCG catalysts.

image of OCG-800 with an interlayer lattice spacing of ~0.39 nm (Fig. 1c). These narrow ridge regions are important for maintaining the 3D structure of OCG particles during solution processing.[39,40]

The stacking structure of OCG particles was further analyzed using X-ray diffraction (XRD). OCG-250 showed a relatively sharp (002) diffraction peak at $2\theta = 11.6^\circ$ with an interplanar spacing of 0.76 nm (Fig. S3, ESI†). Compared to OCG-250, the (002) peaks of OCG-500, OCG-800, and OCG-1000 gradually shifted towards higher diffraction angles, and their interplanar spacings were reduced to 0.40, 0.36, and 0.34 nm, respectively. The reduced interlayer distance can be attributed to the removal of oxygen functional groups at higher temperatures. The surface defect structure of the OCGs was studied using Raman spectroscopy (Fig. 1d). All OCGs showed a broad D peak at ~1360 cm^{-1}, in addition to a sharp G peak at ~1580 cm^{-1}, revealing the incorporation of structural defects in the sp^2-hybridized carbon systems. The integrated ratio of D to G peak (A_G/A_D) was calculated to be 0.74, 0.71, 0.67, and 0.65 for OCG-250, OCG-500, OCG-800, and OCG-1000, respectively. This indicates that higher reduction temperatures form more defects on the graphene surface. The thermal reduction of

oxygen functional groups is accompanied by the generation of O_2, CO, and CO_2 products,[41] causing the formation of more defect sites. This intensity ratio was further used to define the amount of defects in the radar plot.

The chemical structure and composition of OCG particles were characterized by X-ray photoelectron spectroscopy (XPS). The XPS survey scans showed reduced oxygen to carbon ratios (O/C) with increasing heating temperatures: 0.49 for OCG-250, 0.22 for OCG-500, 0.16 for OCG-800, and 0.11 for OCG-1000 (Fig. 1e). The XPS high-resolution C1s spectra of OCG catalysts can be fitted by 284.5 eV ± 0.1 eV for sp^2–C (C═C), 285.2 ± 0.2 eV for sp^3–C (C–C), 286.5 ± 0.2 eV for C–O, 288.4 ± 0.1 eV for C═O, and 290.2 ± 0.2 eV for COOH (Fig. 1f). A comparison of the C1s spectra illustrates that the graphene sp^2–C system gradually recovers through the removal of oxygen functional groups at higher temperatures. Interestingly, the dominant epoxide group in OCG-250 was effectively removed in the OCGs synthesized at higher temperatures (≥500 °C). Fourier transform infrared spectroscopy (FTIR) analysis further supported this decreasing trend in the amount of oxygen functional groups with higher reduction temperatures (Fig. S4, ESI†). In addition, O1s XPS spectra of OCG catalysts were deconvoluted by 531.5 eV for O_I (C═O group), 532.7 ± 0.1 eV for O_{II} (C–O–C or COOH group), 534 ± 0.1 eV for O_{III} (C–O(H) group), and 536 ± 0.1 eV for O_{IV} (absorbed H_2O or O_2, Fig. 1g). OCG-250 exhibited a predominant O_{II} species over other oxygen functional groups, but the O_{II} species progressively decreased with increasing annealing temperatures (Fig. 1h and Table S1, ESI†). These results indicate that the physical and chemical structures of OCG, including surface defects and oxygen functional groups, can be effectively controlled by adjusting the reduction temperature (Fig. 1i), which provides an important model system for studying the structure-mechanism-performance relationship of graphene catalysts for the $2e^-$ ORR.

Electrocatalytic ORR performance of OCG catalysts

The electrochemical active surface area (ECSA) of the OCG catalysts was compared by measuring their double-layer capacitance (C_{dl}) using rate-dependent cyclic voltammetry (CV) scans (Fig. S5 and S6, ESI†). The C_{dl} values of OCG catalysts increased with increasing annealing temperature—from 1.88 mF cm^{-2} for OCG-250 to 2.54 mF cm^{-2} for OCG-1000. The increase in ECSA at higher temperatures may be attributed to the increased number of defect sites on the surface of graphene. The ORR performance of the OCG catalysts was evaluated using a 3-electrode cell with a rotating ring-disk electrode (RRDE) at 1600 rpm in O_2-saturated 0.1 M KOH. The collection efficiency (N = 0.25) was pre-calibrated using the reversible $[Fe(CN)_6]^{4-/3-}$ redox couple (Fig. S7, ESI†). The ORR polarization curves for the OCG catalysts with the oxygen reduction current density at the disk electrode (solid line), and the H_2O_2 oxidation current density at the ring electrode (dashed line) are shown in Fig. 2a. The corresponding H_2O_2 selectivity and transference number (n) were calculated over a

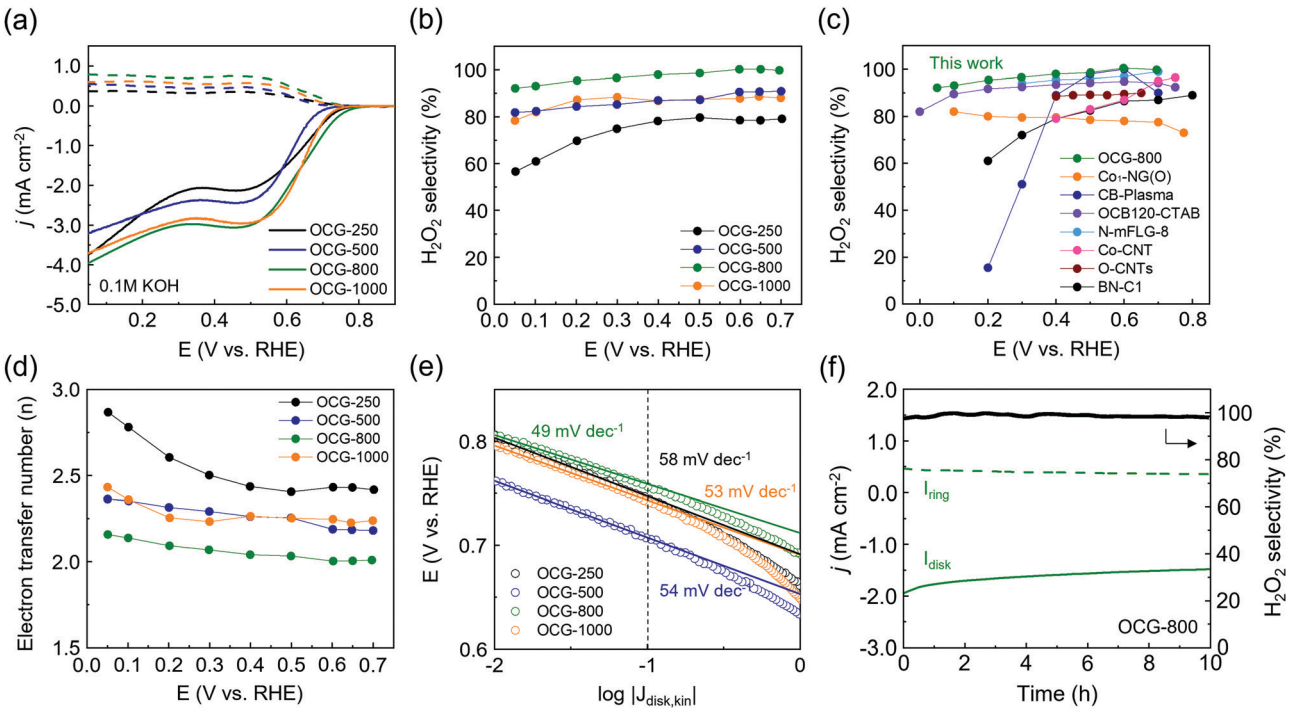

Fig. 2 (a) Comparison of ORR performance of OCG catalysts at 1600 rpm and a rate of 10 mV s^{-1}, representing the ORR current density at the disk electrode (solid line) and the detected H_2O_2 current density at the ring electrode (dash line) in O_2-saturated 0.1 M KOH. (b) The calculated H_2O_2 selectivity of OCG catalysts, (c) comparison of selectivity and potential window among previously reported catalysts, and (d) the calculated electron transfer number of OCG catalysts. (e) The calculated Tafel plots of OCG catalysts. (f) Chronoamperometry stability test of OCG-800 at 0.65 V *vs.* RHE in O_2-saturated 0.1 M KOH.

wide potential window from 0.05 to 0.7 V *vs.* RHE. OCG-800 maintained a high H_2O_2 selectivity of >92% over the entire potential, while OCG-500 and OCG-1000 exhibited a reduced H_2O_2 selectivity of 82–90%, and OCG-250 showed the lowest H_2O_2 selectivity of 60–78% (Fig. 2b). Notably, OCG-800 showed the excellent H_2O_2 selectivity of 100% at 0.6 and 0.65 V *vs.* RHE. It should be noted that OCG-800 exhibited the highest selectivity in the wide range of 0.05 to 0.7 V *vs.* RHE among previously reported carbon-based and metal-embedded electrocatalysts (Fig. 2c).[25,32,33,35,36,42,43] The calculated n value of OCG-800 from the disk and ring current was the closest to 2.0, further supporting its higher suitability for the $2e^-$ reaction compared to other OCG catalysts (Fig. 2d). These results were in good agreement with the values of n obtained according to the Koutechy–Levich equation using a rotating disk electrode (RDE) (Fig. S8, ESI†). The calculated Tafel slope of OCG-800 (49 mV dec^{-1}) was also much lower than those of the other OCG catalysts, indicating the faster reaction kinetics of OCG-800 (Fig. 2e). This outstanding electrochemical performance of OCG-800 can be attributed to the facilitated mass transfer of the reactants to the active sites on the 3D-structured graphene surface containing optimized oxygen functional groups and defect sites. It should be noted that ORR performance is more closely related to oxygen functional group content and defect structure than ECSA (Fig. S9, ESI†). OCG-1000 with the highest ECSA exhibited a similar activity to OCG-500, supporting the importance of the combination of functional groups and defect structures. In addition, the amount of catalyst loaded on the glass carbon (GC) disk electrode can be an important factor for the ORR performance. Therefore, the optimal loading was determined by varying the loading amount of OCG-800 from 5 to 50 μg cm^{-2}, and it was found that a loading amount of 10 μg cm^{-2} delivered optimal H_2O_2 activity and selectivity (Fig. S10, ESI†). Furthermore, the stability of the OCG-800 catalyst was demonstrated by a chronoamperometry (CA) test for 10 h with an average H_2O_2 selectivity of 98% (Fig. 2f). In addition to the excellent performance of OCG-800 in alkaline media, a high selectivity of ~88% was achieved in a neutral solution (0.5 M NaCl and Fig. S11, ESI†). The 0.5 M NaCl electrolyte represents seawater that can be utilized in various energy fields.[44–47] This result suggests that seawater can be a promising resource as an electrolyte for large-scale, cost-effective electrochemical production of H_2O_2.[29,48–51]

The kinetic current density of OCG-800 for H_2O_2 production was obtained according to eqn (S2) and (S3) (ESI†) in the Experimental section to compensate for the mass-transport limitation. OCG-800 exhibited a kinetic current density of 3.2 mA cm^{-2}_{RDE} (at 0.65 V *vs.* RHE) and a mass activity of 158 A g^{-1} (at 0.65 V *vs.* RHE), surpassing the state-of-the-art catalysts (Fig. 3a).[17,25,33,35,36,42,43] In addition, the H_2O_2 production yield of OCG catalysts was measured in the H-cell configuration, and the yield rate was normalized by the catalyst loading amount (~0.78 mg cm^{-2}, Fig. 3b). The generated H_2O_2 concentrations were estimated by calibrating the titration method *via* UV-visible spectroscopy (Fig. S12, ESI†). OCG-800 showed the highest H_2O_2 productivity of 473.9 (±29) mmol g_{cat}^{-1} h^{-1} at

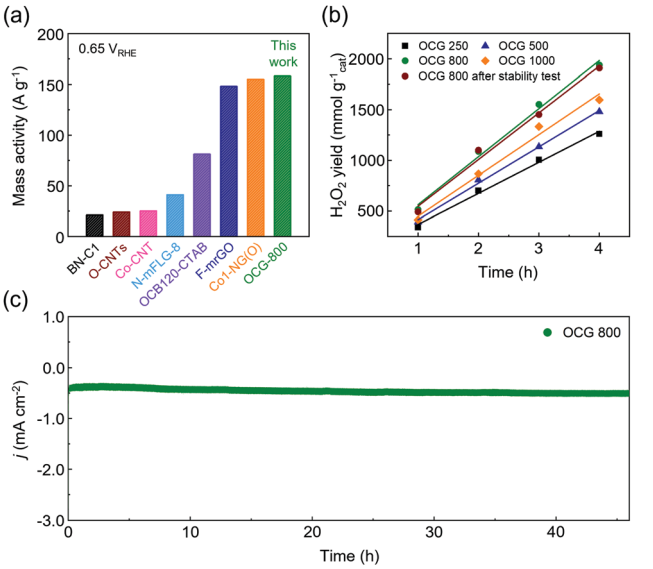

Fig. 3 (a) Comparison of mass activity at 0.65 V *vs.* RHE between OCG-800 and previously reported catalysts under alkaline media, normalized by the entire mass of the catalyst. (b) H_2O_2 yield of OCG-250, OCG-500, OCG-800 before/after the stability test and OCG-1000 catalysts over different reaction times, applied by 0.4 V *vs.* RHE electrolysis in H-cell. (c) Stability of OCG-800 after continuous operations by chronoamperometric test at 0.4 V *vs.* RHE.

0.4 V *vs.* RHE. This H_2O_2 production rate is higher than any previously reported metal-free catalyst (Table S2, ESI†). Furthermore, the OCG-800 electrode showed excellent stability over 46 h at 0.4 V *vs.* RHE, and the production rate in the alkaline solution was reduced by only 2.8% (460.6 (±35) mmol g_{cat}^{-1} h^{-1}). After the stability test, OCG-800 retained its original 3D morphology and defect structure, further confirming its structural stability (Fig. 3c and Fig. S13, ESI†). In addition, the current density-dependent chronopotentiometry test showed the stable operation of OCG-800 even at 60 mA cm^{-2} in H-cell, suggesting the potential for stable H_2O_2 production *via* the electrochemical synthesis route (Fig. S14, ESI†).

The catalytic active sites for H_2O_2 synthesis

The experimental results demonstrate that the annealing process of OCG catalysts can optimize the structures of the catalytic active sites of graphene by controlling oxygen functional groups and defect sites. To identify the catalytic active sites for H_2O_2 production in terms of the functional groups and defects in the OCG, DFT calculations were systematically performed. As shown in Fig. 4a and Fig. S15 (ESI†), various oxygen functional groups of the graphene model system, such as epoxide, carbonyl (C=O), ether (C–O–C), carboxyl (COOH), and hydroxyl (C–OH) in the basal planes and edge sites, were considered.[35,52,53] Both basal plane and edge structures with various local environments were used. The first step in the ORR to produce H_2O_2 ($2e^-$ pathway) and H_2O ($4e^-$ pathway) is the protonation of O_2 (OOH*). Therefore, the binding energy of the oxygen intermediate (OOH*, ΔG_{OOH^*}) has been used as a major descriptor to predict the catalytic activity and selectivity in a

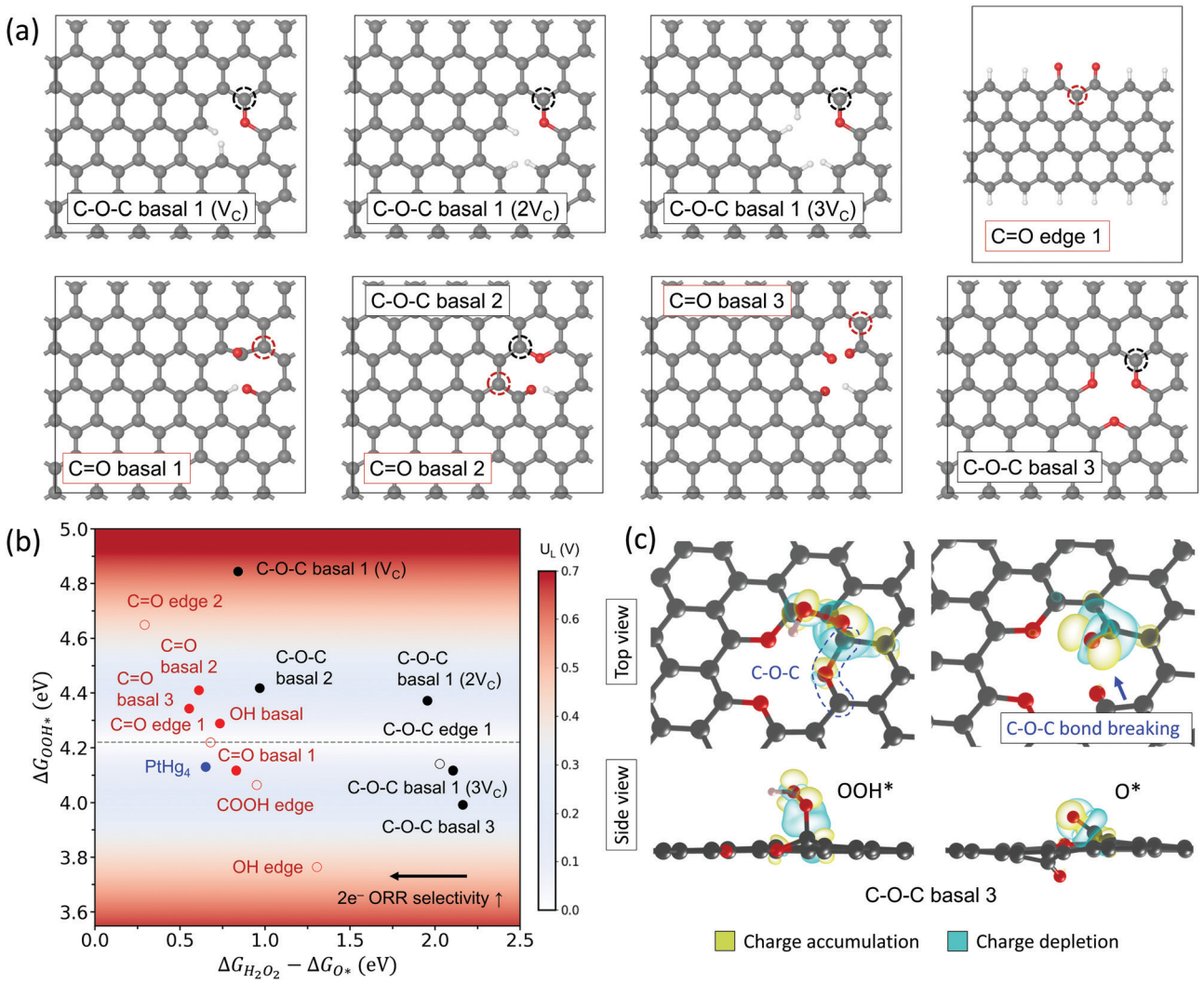

Fig. 4 DFT results of the ORR activity and selectivity of different oxygen functional groups. (a) Model systems of different oxygen functional groups examined in this study. Black and red circles indicate the active site of the C–O–C type and the other functional groups, respectively. Gray, red, and white balls denote C, O, and H atoms, respectively. (b) Scaling relationship between ΔG_{OOH*} and $\Delta G_{H2O2*}-\Delta G_{O*}$ of different oxygen functional groups. The color bar indicates the overpotential as a function of ΔG_{OOH*}. The closed and open circles represent the basal and edge model systems, respectively. The gray dashed line indicates the optimum ΔG_{OOH*} for O_2/H_2O_2 reaction. (c) The blue circle displays the result of $PtHg_4$ adapted from ref. 54. Calculated charge density difference of OOH* and O* on C–O–C basal 3. (Isosurface level: 0.03 e Å^{-3}).

volcano plot.[14,25] The limiting potential (U_L), which is the lowest potential at which all reaction steps are downhill in free energy, was calculated as a function of ΔG_{OOH*} (color map in Fig. 4b). The black and red circles in Fig. 4b indicate the ether groups and other oxygen functional groups respectively. In the ether group, the carbon atom adjacent to oxygen is the active site (black circle in Fig. 4a), showing moderate OOH adsorption strength and a small overpotential for H_2O_2 production. In addition, OOH was more strongly adsorbed as the local defect level near the active site increased, and C–O–C basal 1 ($3V_C$) showed optimal OOH adsorption for the $2e^-$ ORR (Fig. 4b). Conversely, the epoxide group (without carbon defects), which is mainly detected in OCG-250, has very weak OOH adsorption (ΔG_{OOH*} = 5.247 eV) and it is difficult to generate H_2O_2. Carbonyl species (O_I) showed proper OOH* strength regardless of the degree of carbon defects.[52,53] However, the hydroxyl (O_{III}) group exhibited a strong adsorption of OOH as the number of defects increased, resulting in reduced activity. As a result, considering only the first reaction step (OOH*), C═O and defective C–O–C functional groups favored the formation of H_2O_2.

In the next reduction reaction step, the pathway is divided into $2e^-$ ORR and $4e^-$ ORR according to the oxygen adsorption strength (ΔG_{O*}) as follows:

$$OOH^* + (H^+ + e^-) \leftrightarrow * + H_2O_2 \quad (3)$$

$$OOH^* + (H^+ + e^-) \leftrightarrow O^* + H_2O \quad (4)$$

The weak adsorption of O* makes H_2O_2 formation energetically more favorable and improves H_2O_2 selectivity.[54] Therefore,

we first suggested that the selectivity of functionalized carbon catalysts can be predicted based on the scaling relation between ΔG_{OOH^*} and ΔG_{H2O2^*}–ΔG_{O^*} (Fig. 4b). All functional groups except ether (red circle in Fig. 4b) had a weak oxygen adsorption tendency and showed good performance in terms of selectivity. In particular, the carbon atoms adjacent to the C=O functional groups, such as C=O edge 1 and C=O basal 2 and 3, were found to be advantageous in terms of selectivity for $2e^-$ ORR due to the weak oxygen adsorption energy. In addition, these activity sites maintained their initial structure after oxygen adsorption (Fig. S16 and S17, ESI†). In contrast, the O* state of the ether group was excessively stable by breaking the C–O–C bond to form a stable C=O bond (Fig. 4c and Fig. S17, ESI†). This additional C=O bond formation serves as a driving force for strong oxygen adsorption to the ether. All other functional groups retained their initial configuration, even in the O* state. Furthermore, the free energy diagram showed that both C=O and C–O–C have suitable OOH adsorption energies for H_2O_2 production, whereas C–O–C tends to proceed to $4e^-$ ORR due to strong oxygen adsorption (Fig. S18 and Table S3, ESI†). Therefore, considering both the activity (OOH adsorption strength) and selectivity (O adsorption strength), the best performance of OCG-800 can be attributed to the combination of optimal defect structures and C=O functional groups. Moreover, the results demonstrate that the systematic control of surface defects and functional groups can be effectively applied to the design of metal-free carbon catalysts, maximizing both activity and selectivity.

Conclusions

3D graphene catalysts with controlled oxygen functional groups and defects were successfully synthesized using the one-step aerosol spray drying process. The systematic correlation between the structure and electrochemical performance of the graphene catalysts revealed the important role of oxygen functional groups and defects in the effective production of H_2O_2. The graphene catalyst with optimized oxygen functional groups and defect sites, OCG-800, exhibited outstanding H_2O_2 selectivity (92–100%) over a wide potential range with excellent stability. In addition, OCG-800 achieved a high H_2O_2 production rate of 473.9 (±29) mmol g_{cat}^{-1} h^{-1} at 0.4 V *vs.* RHE. Furthermore, DFT calculations revealed the contribution of various oxygen functional groups and defect sites to the $2e^-$ ORR pathway through the scaling relation between OOH and O adsorption strengths. The established structure-mechanism-performance relationship of the nanostructured carbon system for $2e^-$ ORR provides important insights for designing highly active and selective metal-free carbon electrocatalysts for the production of H_2O_2 by fine-tuning oxygen functional groups and defect structures.

Author contributions

K. Lee, J. Lim, M. C. Hatzell, J. Kang and S. W. Lee conceived ideas and designed experiments; M. J. Lee, K. Ryu, and H. Lee helped to characterize the materials; J. Y. Kim, H. Ju, H. S. Cho, and B. H. Kim contributed on the electrochemical analysis; J. Kang conducted the theoretical computations; K. Lee, J. Lim, M. C. Hatzell, J. Kang and S. W. Lee prepared the manuscript. All authors reviewed the manuscript.

Conflicts of interest

There are no conflicts to declare.

Acknowledgements

This work was supported by the Korea Institute of Energy Technology Evaluation and Planning (KETEP) grant funded by the Korea government (MOTIE) (No. 20188550000440). This material is based upon work supported by the National Science Foundation under Grant no. 1751693. This work was performed in part at the Georgia Tech Institute for Electronics and Nanotechnology, a member of the National Nanotechnology Coordinated Infrastructure (NNCI), which is supported by the National Science Foundation (ECCS-2025462). This research was also supported by the Hydrogen Energy Innovation Technology Development Program of the National Research Foundation of Korea (NRF) funded by the Korean government (NRF-2019M3E6A1064020) and the National Institute of Supercomputing and Network/Korea Institute of Science and Technology Information with supercomputing resources including technical support (KSC-2021-CRE-0568).

References

1 G.-h Moon, W. Kim, A. D. Bokare, N.-e Sung and W. Choi, *Energy Environ. Sci.*, 2014, **7**, 4023–4028.
2 S. C. Perry, D. Pangotra, L. Vieira, L.-I. Csepei, V. Sieber, L. Wang, C. Ponce de León and F. C. Walsh, *Nat. Rev. Chem.*, 2019, **3**, 442–458.
3 S. Kato, J. Jung, T. Suenobu and S. Fukuzumi, *Energy Environ. Sci.*, 2013, **6**, 3756–3764.
4 S. Yang, A. Verdaguer-Casadevall, L. Arnarson, L. Silvioli, V. Čolić, R. Frydendal, J. Rossmeisl, I. Chorkendorff and I. E.-L. Stephens, *ACS Catal.*, 2018, **8**, 4064–4081.
5 E. Jung, H. Shin, W. Hooch Antink, Y.-E. Sung and T. Hyeon, *ACS Energy Lett.*, 2020, **5**, 1881–1892.
6 H. Sheng, A. N. Janes, R. D. Ross, D. Kaiman, J. Huang, B. Song, J. R. Schmidt and S. Jin, *Energy Environ. Sci.*, 2020, **13**, 4189–4203.
7 Z. Wei, M. Liu, Z. Zhang, W. Yao, H. Tan and Y. Zhu, *Energy Environ. Sci.*, 2018, **11**, 2581–2589.
8 S. A. Mousavi Shaegh, N.-T. Nguyen, S. M. Mousavi Ehteshami and S. H. Chan, *Energy Environ. Sci.*, 2012, **5**, 8225–8228.
9 Hydrogen Peroxide Global Market Trajectory & Analytics, **https://www.strategyr.com/market-report-hydrogen-peroxide-forecasts-global-industry-analysts-inc.asp**, access Jan, 2022.

10 J. K. Edwards, B. Solsona, N. Edwin Ntainjua, A. F. Carley, A. A. Herzing, C. J. Kiely and G. J. Hutchings, *Science*, 2009, **323**, 1037–1041.
11 S. J. Freakley, Q. He, J. H. Harrhy, L. Lu, D. A. Crole, D. J. Morgan, E. N. Ntainjua, J. K. Edwards, A. F. Carley, A. Y. Borisevich, C. J. Kiely and G. J. Hutchings, *Science*, 2016, **351**, 965–968.
12 Y. Yi, J. Zhou, H. Guo, J. Zhao, J. Su, L. Wang, X. Wang and W. Gong, *Angew. Chem., Int. Ed.*, 2013, **52**, 8446–8449.
13 J. S. Jirkovský, I. Panas, E. Ahlberg, M. Halasa, S. Romani and D. J. Schiffrin, *J. Am. Chem. Soc.*, 2011, **133**, 19432–19441.
14 S. Siahrostami, A. Verdaguer-Casadevall, M. Karamad, D. Deiana, P. Malacrida, B. Wickman, M. Escudero-Escribano, E. A. Paoli, R. Frydendal, T. W. Hansen, I. Chorkendorff, I. E.-L. Stephens and J. Rossmeisl, *Nat. Mater.*, 2013, **12**, 1137–1143.
15 Z. Zheng, Y. H. Ng, D. W. Wang and R. Amal, *Adv. Mater.*, 2016, **28**, 9949–9955.
16 Y. Jiang, P. Ni, C. Chen, Y. Lu, P. Yang, B. Kong, A. Fisher and X. Wang, *Adv. Energy Mater.*, 2018, **8**, 1801909.
17 H. W. Kim, M. B. Ross, N. Kornienko, L. Zhang, J. Guo, P. Yang and B. D. McCloskey, *Nat. Catal.*, 2018, **1**, 282–290.
18 S. Chen, Z. Chen, S. Siahrostami, T. R. Kim, D. Nordlund, D. Sokaras, S. Nowak, J. W.-F. To, D. Higgins, R. Sinclair, J. K. Nørskov, T. F. Jaramillo and Z. Bao, *ACS Sustainable Chem. Eng.*, 2018, **6**, 311–317.
19 V. Viswanathan, H. A. Hansen, J. Rossmeisl and J. K. Nørskov, *J. Phys. Chem. Lett.*, 2012, **3**, 2948–2951.
20 J. K. Nørskov, J. Rossmeisl, A. Logadottir, L. Lindqvist, J. R. Kitchin, T. Bligaard and H. Jónsson, *J. Phys. Chem. B*, 2004, **108**, 17886–17892.
21 D. Kim, H. Nam, Y. H. Cho, B. C. Yeo, S. H. Cho, J. P. Ahn, K. Y. Lee, S. Y. Lee and S. S. Han, *ACS Catal.*, 2019, **9**, 8702–8711.
22 C. H. Choi, M. Kim, H. C. Kwon, S. J. Cho, S. Yun, H. T. Kim, K. J.-J. Mayrhofer, H. Kim and M. Choi, *Nat. Commun.*, 2016, **7**, 10922.
23 Y. L. Wang, S. Gurses, N. Felvey, A. Boubnov, S. S. Mao and C. X. Kronawitter, *ACS Catal.*, 2019, **9**, 8453–8463.
24 A. Verdaguer-Casadevall, D. Deiana, M. Karamad, S. Siahrostami, P. Malacrida, T. W. Hansen, J. Rossmeisl, I. Chorkendorff and I. E.-L. Stephens, *Nano Lett.*, 2014, **14**, 1603–1608.
25 E. Jung, H. Shin, B. H. Lee, V. Efremov, S. Lee, H. S. Lee, J. Kim, W. Hooch Antink, S. Park, K. S. Lee, S. P. Cho, J. S. Yoo, Y. E. Sung and T. Hyeon, *Nat. Mater.*, 2020, **19**, 436–442.
26 F. Luo, A. Roy, L. Silvioli, D. A. Cullen, A. Zitolo, M. T. Sougrati, I. C. Oguz, T. Mineva, D. Teschner, S. Wagner, J. Wen, F. Dionigi, U. I. Kramm, J. Rossmeisl, F. Jaouen and P. Strasser, *Nat. Mater.*, 2020, **19**, 1215–1223.
27 H. Fei, J. Dong, Y. Feng, C. S. Allen, C. Wan, B. Volosskiy, M. Li, Z. Zhao, Y. Wang, H. Sun, P. An, W. Chen, Z. Guo, C. Lee, D. Chen, I. Shakir, M. Liu, T. Hu, Y. Li, A. I. Kirkland, X. Duan and Y. Huang, *Nat. Catal.*, 2018, **1**, 63–72.
28 Y. Sun, L. Silvioli, N. R. Sahraie, W. Ju, J. Li, A. Zitolo, S. Li, A. Bagger, L. Arnarson, X. Wang, T. Moeller, D. Bernsmeier, J. Rossmeisl, F. Jaouen and P. Strasser, *J. Am. Chem. Soc.*, 2019, **141**, 12372–12381.
29 Q. Zhao, Y. Wang, W.-H. Lai, F. Xiao, Y. Lyu, C. Liao and M. Shao, *Energy Environ. Sci.*, 2021, **14**, 5444–5456.
30 T. Yu and C. B. Breslin, *J. Electrochem. Soc.*, 2020, **167**, 126502.
31 Y. J. Sa, J. H. Kim and S. H. Joo, *Angew. Chem., Int. Ed.*, 2019, **58**, 1100–1105.
32 Z. Wang, Q.-K. Li, C. Zhang, Z. Cheng, W. Chen, E. A. McHugh, R. A. Carter, B. I. Yakobson and J. M. Tour, *ACS Catal.*, 2021, **11**, 2454–2459.
33 K.-H. Wu, D. Wang, X. Lu, X. Zhang, Z. Xie, Y. Liu, B.-J. Su, J.-M. Chen, D.-S. Su, W. Qi and S. Guo, *Chem*, 2020, **6**, 1443–1458.
34 Y. Pang, K. Wang, H. Xie, Y. Sun, M.-M. Titirici and G.-L. Chai, *ACS Catal.*, 2020, **10**, 7434–7442.
35 Z. Lu, G. Chen, S. Siahrostami, Z. Chen, K. Liu, J. Xie, L. Liao, T. Wu, D. Lin, Y. Liu, T. F. Jaramillo, J. K. Nørskov and Y. Cui, *Nat. Catal.*, 2018, **1**, 156–162.
36 L. Li, C. Tang, Y. Zheng, B. Xia, X. Zhou, H. Xu and S.-Z. Qiao, *Adv. Energy Mater.*, 2020, **10**, 2000789.
37 M. J. Lee, K. Lee, J. Lim, M. Li, S. Noda, S. J. Kwon, B. DeMattia, B. Lee and S. W. Lee, *Adv. Funct. Mater.*, 2021, **31**, 2009397.
38 J. J. Shao, W. Lv and Q. H. Yang, *Adv. Mater.*, 2014, **26**, 5586–5612.
39 J. Luo, H. D. Jang and J. Huang, *ACS Nano*, 2013, **7**, 1464–1471.
40 B. Lee, M. Kim, S. Kim, J. Nanda, S. J. Kwon, H. D. Jang, D. Mitlin and S. W. Lee, *Adv. Energy Mater.*, 2020, **10**, 1903280.
41 A. Bagri, C. Mattevi, M. Acik, Y. J. Chabal, M. Chhowalla and V. B. Shenoy, *Nat. Chem.*, 2010, **2**, 581–587.
42 S. Chen, Z. Chen, S. Siahrostami, D. Higgins, D. Nordlund, D. Sokaras, T. R. Kim, Y. Liu, X. Yan, E. Nilsson, R. Sinclair, J. K. Nørskov, T. F. Jaramillo and Z. Bao, *J. Am. Chem. Soc.*, 2018, **140**, 7851–7859.
43 K. Jiang, S. Back, A. J. Akey, C. Xia, Y. Hu, W. Liang, D. Schaak, E. Stavitski, J. K. Nørskov, S. Siahrostami and H. Wang, *Nat. Commun.*, 2019, **10**, 3997.
44 J. Yu, B.-Q. Li, C.-X. Zhao and Q. Zhang, *Energy Environ. Sci.*, 2020, **13**, 3253–3268.
45 S. M. Hwang, J. S. Park, Y. Kim, W. Go, J. Han, Y. Kim and Y. Kim, *Adv. Mater.*, 2019, **31**, 1804936.
46 K. Mase, M. Yoneda, Y. Yamada and S. Fukuzumi, *Nat. Commun.*, 2016, **7**, 11470.
47 L. Yu, Q. Zhu, S. Song, B. McElhenny, D. Wang, C. Wu, Z. Qin, J. Bao, Y. Yu, S. Chen and Z. Ren, *Nat. Commun.*, 2019, **10**, 5106.
48 Y. C. Kim and M. Elimelech, *J. Membr. Sci.*, 2013, **429**, 330–337.
49 A. Boonserm, C. Kruehong, V. Seithtanabutara, A. Artnaseaw and P. Kwakhong, *Appl. Surf. Sci.*, 2017, **419**, 933–941.
50 A. Politano, P. Argurio, G. Di Profio, V. Sanna, A. Cupolillo, S. Chakraborty, H. A. Arafat and E. Curcio, *Adv. Mater.*, 2017, **29**, 1603504.

51 X. Song, Z. Liu and D. D. Sun, *Energy Environ. Sci.*, 2013, **6**, 1199–1210.
52 G. F. Han, F. Li, W. Zou, M. Karamad, J. P. Jeon, S. W. Kim, S. J. Kim, Y. Bu, Z. Fu, Y. Lu, S. Siahrostami and J. B. Baek, *Nat. Commun.*, 2020, **11**, 2209.
53 S. Chen, T. Luo, K. Chen, Y. Lin, J. Fu, K. Liu, C. Cai, Q. Wang, H. Li, X. Li, J. Hu, H. Li, M. Zhu and M. Liu, *Angew. Chem., Int. Ed.*, 2021, **60**, 16607–16614.
54 S. Back, J. Na and Z. W. Ulissi, *ACS Catal.*, 2021, **11**, 2483–2491.